NANO · MICRO small
www.small-journal.com

Simple I-Shaped Aryl-Based Dyes for Tin Perovskite Solar Cells with Selenophene Core Moiety as Self-Assembled Monolayers on NiOx Using Two-Step Fabrication

Yun-Sheng Shih, Arulmozhi Velusamy, Chun-Hsiao Kuan, Pei-Yu Huang, Che-Hsin Kuo, De-You Zeng, Cheng-Liang Liu, Shao-Huan Hong, Xianyuan Jiang, Ming-Chou Chen, and Eric Wei-Guang Diau**

Six novel organic small molecules, TPA-Sp-PA (1), TPA-Sp-PE (1E), TPA-T-PA (2), TPA-T-PE (2E), TPA-P-PA (3) and TPA-P-PE (3E) are developed and applied to NiOx films as self-assembled monolayers (SAMs) for tin perovskite solar cells (TPSCs). The linker between acceptor (phosphonic acid (PA) or phosphonic ester (PE)) and donor (triphenylamine (TPA)) plays an important role in facilitating the growth of high-quality perovskite films using a two-step method. Three different types of linkers, phenyl ring (P), thiophene (T), and selenophene (Sp), are studied, for which the Sp-based SAMs provide the best device performance with TPA-Sp-PE (1E) achieving a PCE 8.7%, and its acidic analog, TPA-Sp-PA (1), reaching a maximum PCE of 8.3%. Single crystal structures of TPA-Sp-PE (1E) and TPA-T-PE (2E) are successfully obtained, with the expectation that a uniform SAM would form on the NiOx/ITO substrate. The research introduces a novel approach to enhance TPSC performance by integrating organic SAMs with NiOx HTMs, offering a promising avenue for future progress in TPSC technology through a two-step fabrication technique.

1. Introduction

Perovskite solar cells (PSCs) have received substantial interest in the last 10 years due to their notable benefits, such as solution processability, low manufacturing costs, and remarkable power conversion efficiency (PCE).[1] PSCs have recently achieved a PCE of 26.7%,[2,3] highlighting their potential as the next-generation photovoltaic technology.[4] Hole transport materials (HTMs) are essential for effectively enabling electron-hole pair dissociation in PSCs by conveying holes while obstructing electrons.[5–7] NiOx,[8,9] poly[bis(4-phenyl)(2,4,6-trimethylphenyl)amine] (PTAA),[10,11] and poly-(3,4-ethylene dioxythiophene):poly(4-styrenesulfonate) (PEDOT:PSS)[12–14] are commonly used HTMs for inverted planar PSCs. To obtain homogeneous films, these HTMs usually

Y.-S. Shih, C.-H. Kuan, P.-Y. Huang, C.-H. Kuo, E. W.-G. Diau
Department of Applied Chemistry and Institute of Molecular Science
National Yang Ming Chiao Tung University
1001 Ta-Hseuh Rd., Hsinchu 300093, Taiwan
E-mail: diau@nycu.edu.tw

A. Velusamy, D.-Y. Zeng, M.-C. Chen
Department of Chemistry and Research Center of New Generation Light Driven Photovoltaic Modules
National Central University
Taoyuan 32001, Taiwan
E-mail: mcchen@ncu.edu.tw

C.-L. Liu, S.-H. Hong
Department of Materials Science and Engineering
National Taiwan University
Taipei 10617, Taiwan

X. Jiang
School of Physical Science and Technology
ShanghaiTech University
Shanghai 201210, China

E. W.-G. Diau
Center for Emergent Functional Matter Science
National Yang Ming Chiao Tung University
1001 Ta-Hseuh Rd., Hsinchu 300093, Taiwan

The ORCID identification number(s) for the author(s) of this article can be found under https://doi.org/10.1002/smll.202500642

DOI: 10.1002/smll.202500642

need to be deposited at a thickness of only a few nanometers. Additionally, for effective charge transport, their HOMO levels and hole mobilities must be properly tuned.[15–17] In contrast, self-assembled monolayers (SAMs)-based HTMs can be applied in very thin layers on transparent conductive oxide (TCO) electrodes. This can alter the work function of the TCO by generating permanent dipole at the interfaces.[18–21] Furthermore, the presence of anchoring groups in the SAMs interacts strongly with the electrode surfaces, reducing charge recombination at the HTM and perovskite interface. The SAM treatment also produces hydrophobic surfaces that promote perovskite crystal formation and enhance the PSC performance.[22,23]

SAMs generally consist of three components: a head group (donor), a linker (core), and an anchoring (acceptor) group. The anchoring group significantly influences the binding energy to electrode surfaces, as well as affects the charge transport, interfacial dipole moment, and recombination in devices.[24–26] Common anchoring groups include phosphonic acid (PA), carboxylic acid (CA), cyanoacetic acid (CAA), dicyano (MN), boronic acid ($B(OH)_2$), and sulfonic acid (SO_3H). Among these, PA, CA, and CAA are predominantly used for developing SAM-based HTMs in PSCs. Compounds that are hydrophobic and conjugated, such as triphenylamine, carbazole, and phenothiazine, are frequently used as head groups. Connecting the head and anchoring groups is the linker, which can be either an aliphatic or aromatic group.[27] The PA group, in particular, consists of two hydroxyl units and a phosphonic group, enabling it to bind in three different ways based on the surface and reaction parameters.[24] PA exhibits the greatest binding energy with TiO_2 surfaces compared to other anchoring groups.[28] It provides exceptional stability to the SAM, making PA the best anchoring group for SAMs. Consequently, many SAMs incorporating PA have been developed for use as HTMs in PSCs.

So far, several SAMs have been reported using PA as an anchoring group with aliphatic linkers. For example, Magomedov et al. first designed dimethoxydiphenylamine-substituted carbazole **V1036** as a hole-transporting SAM and used as the dopant-free hole-selective contact in Pb-PSCs and obtained a PCE of 17.8%,[29] as shown in **Figure 1a**. Similarly, Ashouri et al. designed and synthesized carbazole-based **2PACz** SAM with a C2 alkyl chain attached to phosphonic acid groups, which exhibited PCE of 20.9% when implemented in the Pb-based inverted PSCs.[30] Li et al. synthesized **TPT-P6** with PA as an anchoring group and a phenothiazine head group, which demonstrated a higher PCE of 22% and greater stability.[31] Ullah et al. developed **Br-2EPT**, a phenothiazine-based SAM that shows minimized nonradiative recombination loss and thus makes it possible to improve PCE up to 22.44%.[32] Additionally, Jiang et al. designed a helical π-expanded carbazole-derivative, **CbzNaph**, which self-assembled into a densely packed and well-ordered monolayer, achieving a maximum PCE of 24.1%.[33] Recently, Wu et al. reported inverted PSCs employing a bisphosphonate-anchored indolocarbazole (IDCz)-derived SAM, **IDCz-3**, as the hole-extraction layer and a champion PCE of 25.15% was achieved.[34] The SAM **MPA-CPA**, reported as the only SAM using cyanovinyl phosphonic acid as the anchoring group without any linker groups achieved a PCE of 25.2%.[35] This amphiphilic SAM was developed by Zhang et al., with a versatile anchoring group cyanovinyl PA that creates a super wetting underlayer for perovskite deposition. This results in high-quality perovskite films with fewer interface defects, leading to **MPA-CPA**-based PSCs with a PCE of over 25% and excellent stability in Pb-PSCs. According to these findings, SAMs with PA/CPA anchoring groups are highly suitable as HTMs for high-performance PSCs.

Currently, tin-based PSCs (TPSCs) are gaining attention as a viable lead-free alternative, having achieved notable PCEs of 15.7%[36] and 15.38%.[37] These results were accomplished by incorporating 4-fluorophenethylamine hydrobromide as an interfacial dipole and isomeric fulleropyrrolidines as additives. While TPSCs still trail behind lead-based perovskites in terms of performance, tin perovskites possess a narrower bandgap compared to lead-based counterparts, indicating the potential for TPSCs to reach a higher theoretical PCE than Pb-PSCs.[38,39] To mitigate issues such as Sn^{2+}/Sn^{4+} oxidation, enhance surface passivation, and control crystal formation in TPSCs, various strategies involving additives have been explored.[40–48] For example, our team recently utilized SAMs of **MeO-2PACz**[49] in TPSCs, resulting in a PCE of 6.5% (Figure 1a). More recently, we developed a **TP-MN** SAM based on a thieno[3,4-b]pyrazine core, which achieved a maximum PCE of 7.7% when combined with NiOx in TPSCs.[50] In addition, our group developed new quinoxaline-based SAMs, **TQx** and **TQxD**, which exhibited PCEs of 8.0% and 8.3%, respectively, in TPSCs.[51] Triphenylamine-based Y-shaped organic sensitizers were also developed, with the **TPAT-CA** achieving a PCE of 8.1% as p-type SAM for TPSCs.[52]

Motivated by these seminal studies and prior investigations, we have developed a series of simple and novel "I-shaped" aryl-based **TPA-Ar** SAMs as highly effective and cost-efficient surface modifiers. These SAMs feature various heterocyclic rings (benzene, thiophene, and selenophene) as aromatic linkers, dimethoxy-substituted triphenylamine groups as donor (head) groups, and cyanovinyl PA and PE as anchoring groups. In contrast to conventional dye-based SAMs, which often involve complex synthesis processes and high material costs, our Ar-based SAMs are straightforward to synthesize and offer significant material cost reductions.[53] This simplicity and affordability make them particularly attractive for large-scale production, where cost-efficiency is critical. The use of simple aryl rings as core moieties in SAMs for TPSCs provides several advantages, including reduced steric hindrance, enhanced charge injection, and improved efficiency. Additionally, these simple aryl rings facilitate better molecular packing and ease of processing.[54,55] Their cost-effectiveness, stability, and ease of functionalization further enhance their potential as an optimal choice for improving TPSC performance.[56]

To achieve high-quality perovskite films, we utilize a two-step spin coating technique to fabricate the tin perovskite layer, as opposed to the traditional one-step method commonly employed by research teams worldwide. While the one-step process is widely used, the rapid crystallization of perovskites makes it challenging to precisely control nucleation and growth, leading to less uniform films. In our two-step approach, we incorporate a cosolvent system as the antisolvent in the second spin coating step. Typically, isopropyl alcohol serves as the antisolvent in this phase, but it can degrade tin perovskite films. To address this, our lab developed a cosolvent system in 2020, combining isopropyl alcohol, hexafluoroisopropanol, and chlorobenzene, which enables the

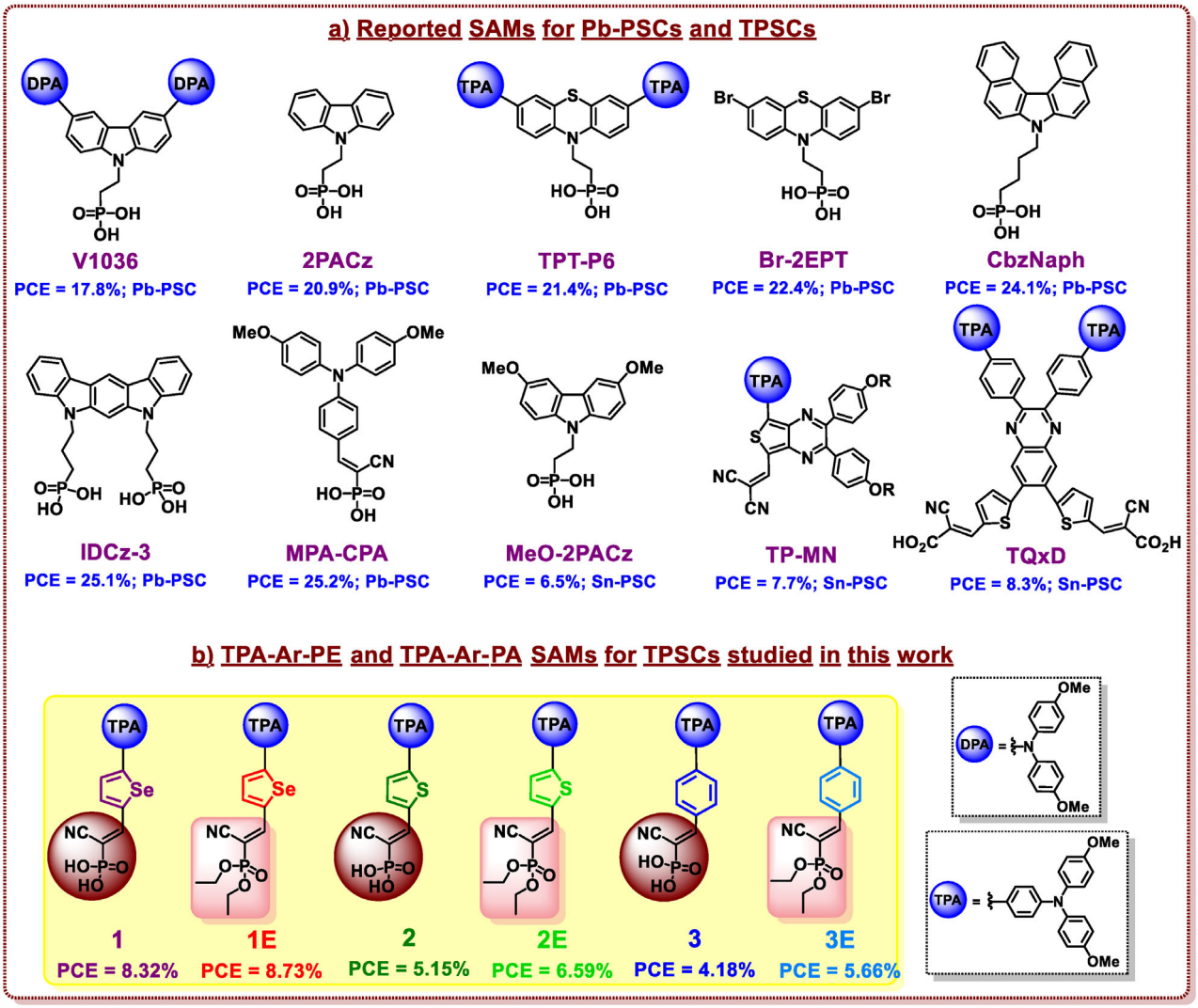

Figure 1. Chemical structures of the a) reported SAMs for Pb-PSCs and TPSCs, and b) **TPA-Ar-PE** and **TPA-Ar-PA** SAM molecules for TPSCs, as presented in this study.

formation of high-quality tin perovskite films.[57] For the SAMs used in this study, the one-step method failed to produce a uniform perovskite film, highlighting the necessity of using a two-step approach to make a TPSC in this study.

Figure 1b depicts the chemical structures of six newly designed and examined SAM molecules in this study: **TPA-Sp-PA** (**1**), **TPA-Sp-PE** (**1E**), **TPA-T-PA** (**2**), **TPA-T-PE** (**2E**), **TPA-P-PA** (**3**) and **TPA-P-PE** (**3E**). In these SAMs, the anchoring groups (PA and PE) are located at one end of the aryl linkers, while the donor moiety, 4,4'-dimethoxytriphenylamine is located at the opposite end. This configuration strengthens the attachment to the NiOx/ITO surface, promoting optimal molecular orientation and better interaction with the perovskite layer. This is supported by the successful formation of single crystals of **TPA-Sp-PE** (**1E**) and **TPA-T-PE** (**2E**) through a slow solvent evaporation technique. Intramolecular interactions within these SAMs aid in creating a consistent and tightly packed monolayer on the NiOx/ITO substrate, enhancing charge transport efficiency. Furthermore, the introduction of this "I-shaped" Ar-based SAM resulted in the highest reported PCE of 8.7% for **TPA-Sp-PE** (**1E**)-based TPSC, with its acidic analog, **TPA-Sp-PA** (**1**), achieving a maximum PCE of 8.3%. These results surpass the performance of previous dye-based SAMs, demonstrating the potential of this cost-effective approach to significantly enhance TPSC performance. The unique molecular design and its well-defined geometry play a crucial role in optimizing the interface between the perovskite layer and the NiOx/ITO substrate, reducing charge recombination and improving charge transport, which ultimately boosts the efficiency of the devices.

2. Results and Discussion

2.1. Synthesis

TPA-Ar-based SAM molecules were synthesized as shown in **Scheme** 1. First, 5-bromoaryl-2-carbaldehydes **4–6** were coupled with stannylated 4,4'-dimethoxy triphenylamine *via* Stille coupling to obtain intermediate aldehydes **7–9** using $Pd(PPh_3)_4$

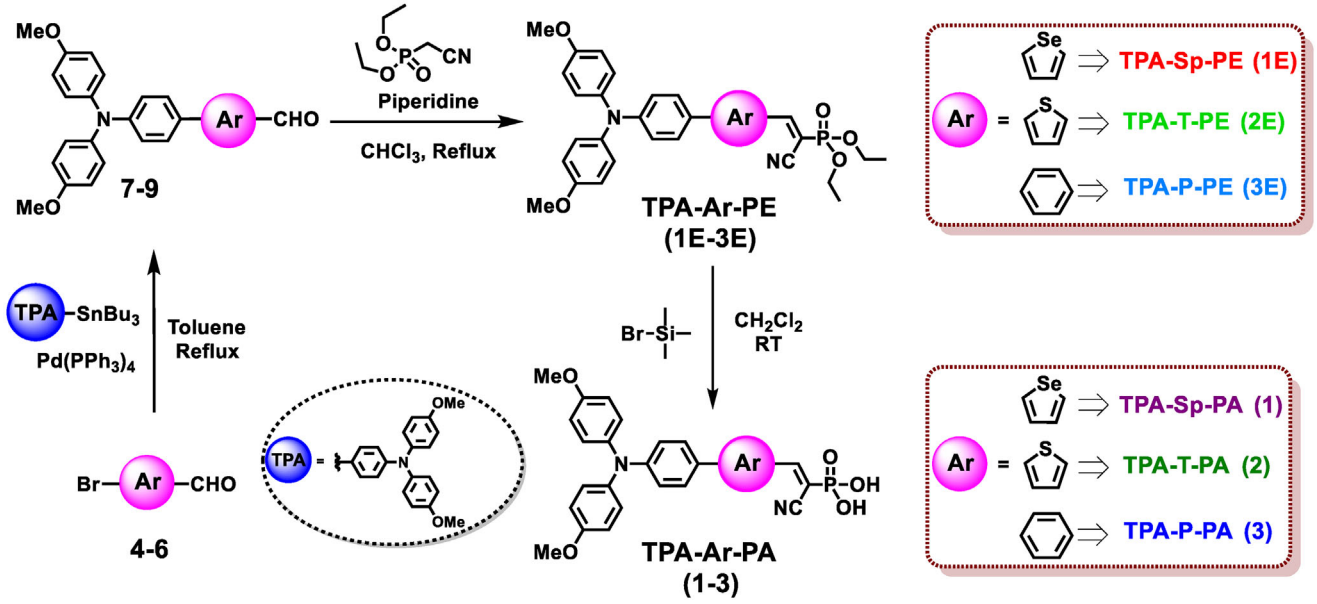

Scheme 1. Synthetic route to **TPA-Ar**-based SAM molecules.

catalyst. Further, a Knoevenagel–Horner reaction between these intermediates and diethyl cyanomethylphosphonate, carried out in the presence of piperidine, under reflux in chloroform gave the **TPA-Ar-PE** compounds (**1E-3E**). Finally, **TPA-Ar-PE** compounds were converted to cyanovinyl phosphonic acid derivatives, **TPA-Ar-PA** (**1-3**), in good yields (>90%). These SAMs demonstrate excellent solubility in chlorobenzene, chloroform, and tetrahydrofuran. Furthermore, structural characterizations of all the final molecules were analyzed using ^{1}H, ^{13}C, and ^{31}P NMR spectroscopy, as well as mass spectrometry (see Figures S1–S26, Supporting Information).

2.2. Physical Characterizations

Table 1 outlines the physical properties of SAM molecules based on **TPA-Ar**. Thermogravimetric analysis (TGA) was used to evaluate the thermal stability of the newly synthesized SAM molecules (Figure S27, Supporting Information). These SAMs exhibit better thermal stability, with ≈5% weight loss occurring at 201/295 °C, 317/295 °C, and 319/302 °C for compounds **1/1E**, **2/2E**, and **3/3E** respectively. All six compounds possess good thermal stability and the results are provided in Table 1. The UV–vis absorption spectra of all **TPA-Ar** SAMs were measured in *o*-dichlorobenzene solutions and are shown in **Figure 2**a. The order of λ_{max} is observed to be selenophene > thiophene > phenyl-based compounds. This trend is due to the increasing ability of the heteroatoms to donate lone pairs into the π-system, thereby reducing the optical energy gap and absorbing at longer wavelengths. Consequently, the order of absorption maxima is **1E** (495 nm) > **2E** (481 nm) > **3E** (439 nm) and **1** (475 nm) > **2** (473 nm) > **3** (430 nm) for **TPA-Ar-PE** and **TPA-Ar-PA**, respectively. At 25 °C in *o*-DCB, differential pulse voltammetry (DPV) was conducted to analyze the electrochemical properties of all **TPA-Ar** SAM molecules (Figure 2b and Figure S28, Supporting Information), employing tetrabutylammonium hexafluorophosphate as the electrolyte. The oxidation potentials of SAMs were calibrated using ferrocene as an internal standard, with the reference potential fixed at +0.64.[58] The HOMO energy levels of **TPA-Ar** SAMs were determined using the equation $E_{HOMO} = -(4.44 + E_{ox})$. The first oxidation potentials of SAMs are located at +0.94 and +0.88 V, resulting in E_{HOMO} values of −5.38 eV and −5.32 eV for **TPA-Ar-PE** and **TPA-Ar-PA**, respectively. The obtained results suggest that variations in chalcogens have a negligible impact

Table 1. Physical properties of **TPA-Ar** SAMs.

Compound	T_d[a] [°C]	T_m[b] [°C]	λ_{max}(sol)[c] [nm]	ΔE_g[d] [eV]	E_{ox}[e] [V]	HOMO[f] [eV]	LUMO[g] [eV]	ΔE_g[h] [eV]
TPA-Sp-PA (1)	201	81	475	2.09	0.88	−5.32	−3.22	2.56
TPA-Sp-PE (1E)	295	174	495	2.12	0.94	−5.38	−3.26	2.62
TPA-T-PA (2)	317	83	473	2.16	0.88	−5.32	−3.11	2.61
TPA-T-PE (2E)	295	146	481	2.18	0.94	−5.38	−3.19	2.68
TPA-P-PA (3)	319	135	430	2.33	0.87	−5.31	−2.99	2.61
TPA-P-PE (3E)	302	68	439	2.34	0.92	−5.36	−3.01	2.72

[a] Measured using TGA; [b] Determined with a melting point apparatus; [c] Assessed in *o*-DCB; [d] Calculated using 1240/λ_{abs} (onset); [e] DPV results in *o*-DCB; [f] HOMO = −(4.44 + E_{ox}) vs. NHE; [g] LUMO = HOMO + ΔE_g; [h] ΔE_g obtained from DFT calculations.

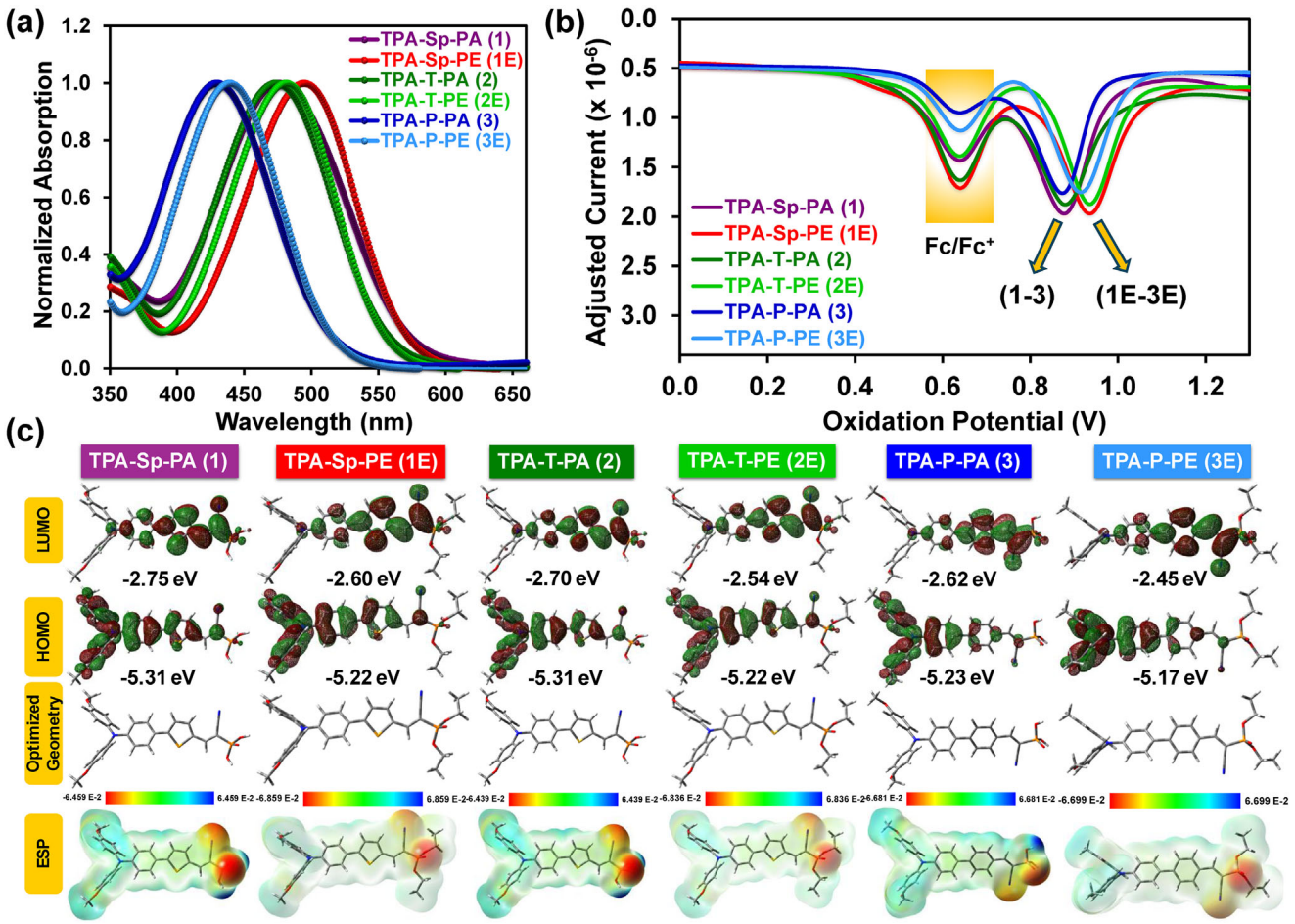

Figure 2. a) UV–vis absorption profiles; b) DPV plots; c) DFT-computed energy levels and ESP visualization for **TPA-Ar** SAMs.

on the electrochemical properties of their corresponding analogs. All three SAMs anchored with cyanovinyl phosphonic acids (PAs; **1–3**) are easier to be oxidized at lower oxidation potentials than their phosphonate (**1E-3E**) analogs, i.e. PAs with higher HOMO than PEs.This can be attributed to the PA group's ability to form hydrogen bonds, which stabilizes the molecule and lowers the overall electron density around the phosphorus atom compared to the PE group. Thus, the electron-withdrawing nature of the PA group might be less effective than that of the PE group. Furthermore, the corresponding E_{LUMO} values are calculated by adding E_{HOMO} to the optical energy gap, and the obtained results are provided in Table 1 and Figure S28 (Supporting Information).

2.3. Theoretical Calculations

DFT calculations at the B3LYP/6-31G* level, performed using the Gaussian 09W program (Figure 2c), were utilized to examine the electronic structures of **TPA-Ar** SAMs. The HOMOs of all the SAM molecules are mainly localized on the triphenylamine units. At the same time, the LUMOs are observed on the aryl groups (selenophene, thiophene, and phenyl) and slightly extended to the cyanovinylene units. The DFT-derived E_{HOMO} and E_{LUMO} of all the compounds range from −5.17 to −5.31 eV and −2.45 to −2.75 eV, respectively. A trend similar to the optical energy gap is observed in the energy gap obtained through DFT calculations: **TPA-Ar-PE** > **TPA-Ar-PA**. Furthermore, an electrostatic potential (ESP) analysis was conducted on **TPA-Ar**-based SAMs to assess the distribution of molecular charges and investigate the NiOx/ITO surface interactions with the sites of anchoring groups (Figure 2c). The DFT analysis and ESP visualization results for the six **TPA-Ar** SAMs show that the phosphonic acid and phosphonate groups have a large concentration of negative charges. This supports the robust interaction with the NiOx/ITO surface, aiding the SAM formation and potentially boosting the transfer of charges at the SAM/NiOx interface in TPSCs.

2.4. Single Crystal Structures

To gain a better understanding of the SAM molecules' structure, single crystals of **TPA-Sp-PE** (**1E**) and **TPA-T-PE** (**2E**) were grown. The single crystal structures, determined through diffraction, are displayed in **Figures** 3 and S29 (Supporting Information), with the corresponding crystal data provided in Tables S1 and S2 (Supporting Information). Both compounds crystallize in the triclinic system with a P-1 space group. Figure 3a,b,e,f show the stick model, while Figure 3c,d,h are presented in the

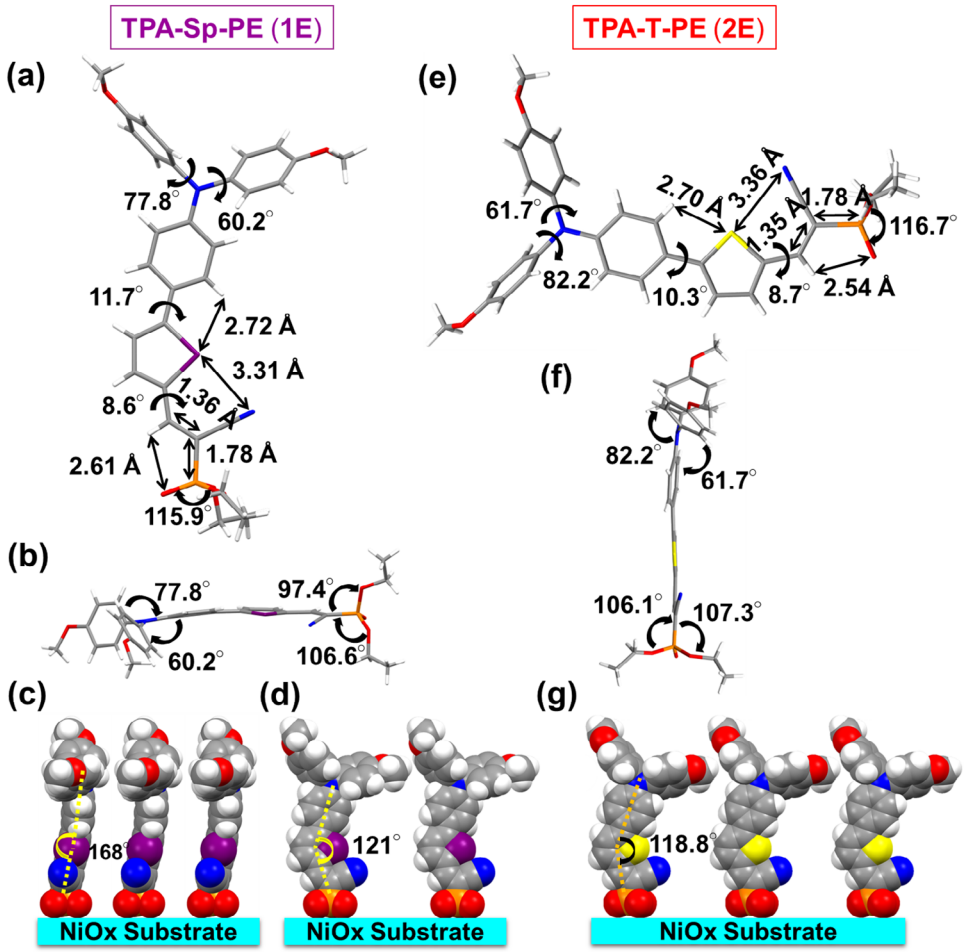

Figure 3. Single crystal structures of **TPA-Sp-PE** (**1E**) and **TPA-T-PE** (**2E**) SAMs. a,e) Top views of molecules **1E** and **2E** showing intramolecular interactions and interplanar angles; b,f) side views of molecules **1E** and **2E** illustrating interplanar angles; c,d,g) proposed packing patterns of the SAMs on a NiOx/ITO substrate (ethyl groups are excluded for clarity). Figure a–d corresponds to **TPA-Sp-PE** (**1E**), while Figure e-g corresponds to **TPA-T-PE** (**2E**).

space-filling model. In Figure 3a, the intramolecular distances are 3.31 Å (Se—N), 2.72 Å (Se—H), and 2.61 Å (O—H), with the SAM molecule oriented vertically, where three oxygen atoms (attached to phosphorus) serve as anchoring points. Figure 3e, in contrast, shows intramolecular distances of 3.36 Å (S—N), 2.70 Å (S—H), and 2.54 Å (O—H). These interactions probably promote the creation of well-ordered SAMs on the substrate, featuring compact and angled textures. As illustrated in Figure 3a,e illustrates the short C═C double bond (≈1.36 Å) between selenophene/thiophene and PE groups, along with a short C– P distance of 1.78 Å. Furthermore, the small interplanar angles of selenophene/thiophene to PA (8.6°/8.7°) and the TPA moiety (11.7°/10.3°) indicate effective π-conjugation between the central selenophene/thiophene and the PE groups, promoting effective charge transfer. Additionally, the larger interplanar angles of **2E** (82.2°/61.7°, as shown in Figure 3e) determined for the phenyl rings in the TPA groups, compared to those of **1E** (77.8°/60.2°, Figure 3a), suggests that **1E** exhibits better planarity, which facilitates charge transport. The wide angles (≈116°; Figure 3a,e) formed by the three oxygen atoms bonded to phosphorus in both compounds likely help the SAM molecules remain firmly anchored to the NiOx substrate. Additionally, Figure 3b,f presents side views of both molecules, highlighting distinct interplanar angles of the phenyl rings, with the P-OEt groups positioned nearly perpendicular to the core plane (97.4°–107.3°). The proposed packing arrangement of **1E** (side and front views) and **2E** (front view) SAM molecules on the NiOx substrate is illustrated in Figure 3c,d,g), contributing to efficient charge transport for greater TPSC performance. The bending angle between the TPA and anchoring units is larger for **1E** (121°, Figure 3d) than **2E** (118.8°, Figure 3g), indicating better molecular linearity of **1E**, which enhances molecular conjugation and enables more SAM molecules to absorb onto the substrate. These results suggest that chalcogen variation affects the structural parameters, and the presence of intramolecular interactions,[55] along with the smallest interplanar angles in compound **1E**, indicates favorable charge transport unless major morphological defects are noted.

2.5. Hole Transport Layer Characterizations

We adopted X-ray photoelectron spectroscopy (XPS) to provide evidence that SAM and nickel oxide nanoparticles (NiOx) are

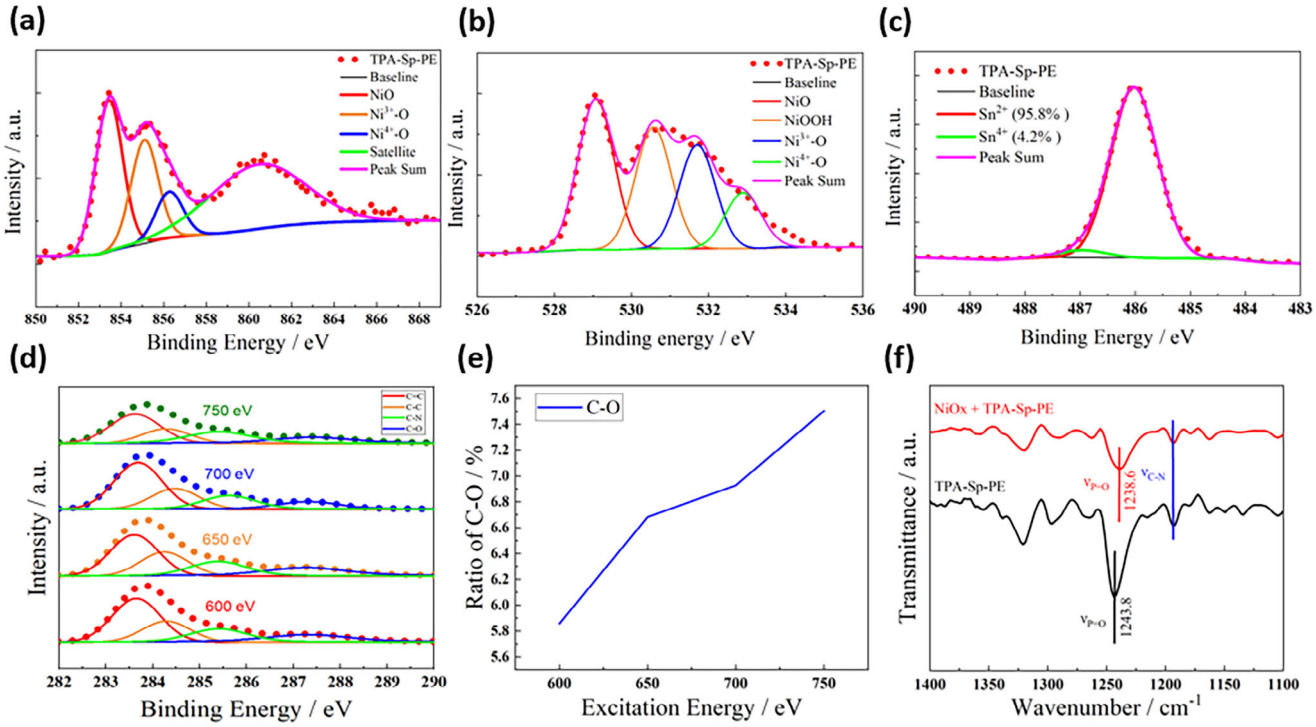

Figure 4. XPS spectra of the **TPA-Sp-PE** (**1E**) compound. a) Nickel spectrum (Ni2p) of **1E** molecule; b) Oxygen spectrum (O1s) of **1E** molecule; c) tin spectrum (Sn3d) of **1E** molecule; d) different excitation energy carbon spectrum (C1s) of **1E** molecule; e) C—O ratio of C1s in different excitation energy f) IR spectrum of **1E** molecule.

indeed bonded to ITO substrates. In order to examine NiOx, we first emphasize the nickel spectra. **TPA-Sp-PE** (**1E**) and other TPA-Ar-based SAM have three peaks at 853.4, 855.1, and 856.3 eV, as shown in **Figures** 4a and S30 (Supporting Information), which correspond to the Ni^{2+}, Ni^{3+}, and Ni^{4+} species, respectively. The Ni^{2+} peak is the main signal of nickel oxide, and Ni^{4+} has a strong oxidizing ability that will destroy tin perovskite films.[59] Ni^{3+} is generated from the nickel vacancy, which is advantageous for the hole transport.[60] The proportions of the three species (Ni^{2+}, Ni^{3+}, Ni^{4+}) within the nickel spectra across all series of SAMs and NiOx-only, as depicted in Table S3 (Supporting Information), clearly indicate that the Ni^{3+} species in the TPA-Ar-based SAMs exceed that of NiOx-only film, while the Ni^{4+} species in the TPA-Ar-based SAMs is found to be lower than that of NiOx-only film. It demonstrates that the SAM-modified NiOx can have a higher Ni^{3+} content, which improves hole transport capacity.

Next, we examine the XPS spectra of oxygen illustrated in Figure 4b and Figure S31 (Supporting Information). This spectrum shows four peaks at 529.1, 530.6, 531.7, and 532.9 eV, corresponding to the species of NiO, NiOOH, Ni^{3+}-O, and Ni^{4+}-O, respectively. The quantity of the NiO, Ni^{3+}-O, and Ni^{4+}-O is in the same order as the Ni^{2+}, Ni^{3+}, and Ni^{4+} species in the nickel spectrum. The discovery of NiOOH not only increases conductivity but also aids in the SAM's connection.[61,62] Even with the SAM confirmation, we may still analyze the perovskite film quality by obtaining the tin spectra. According to Figure 4c and Figure S32 (Supporting Information), **TPA-Sp-PE** can have the highest Sn^{2+}/Sn^{4+} ratio (95.8%), which also implies that the SAM can prevent tin perovskite from oxidization.

We also conduct **TPA-Sp-PE (1E)** XPS spectra at various excitation energies, including 600, 650, 700, and 750 eV. The carbon spectra (C1s) exhibit four peaks at 283.6, 284.4, 285.6, and 287.3 eV, as indicated in Figure 4d. The proportions of the three species (C═C, C—C, C—N, and C—O) within the carbon spectra across all series of SAMs and NiOx-only film, as depicted in Table S4 (Supporting Information). These peaks correspond to the species of C═C, C—C, C—N, and C—O. The peak ratios of the C1s spectra are illustrated in Figure 4e and Figure S33 (Supporting Information). Among the four peak ratios, the C—O ratio increases with energy increasing, as shown in Figure 4e. In theory, we can measure deeper SAM information when the excitation energy increases. Figure 3 shows the single crystal structure of the **TPA-Sp-PE** (**1E**), the PE anchoring group attached to the NiOx is the deepest SAM layer, and only the PE group has the most C—O bonding. Accordingly, the C—O bond ratio will increase as the excitation energy rises, consistent with the results displayed in Figure 4e.

To understand the anchoring effect between the self-assembly monolayer and NiOx, we employed the Fourier Transform Infrared (FTIR) spectroscopic technique. In our study, we employed synchrotron radiation as the light source instead of the conventional IR light source. This synchrotron radiation allows us to reduce the spot size from ≈50×30 μm^2 (as seen with commercial FTIR) to ≈13×10 μm^2, thereby enhancing our spatial resolution. In our specific application, the interaction between **TPA-Sp-PE** (**1E**) and the NiOx surface was studied. The FTIR spectra revealed a redshift of 5.2 cm^{-1} in the P═O stretching vibration as shown in Figure 4f, indicating chelation of **TPA-Sp-PE** (**1E**) to the NiOx surface. Notably, there was no shift observed in the C—N

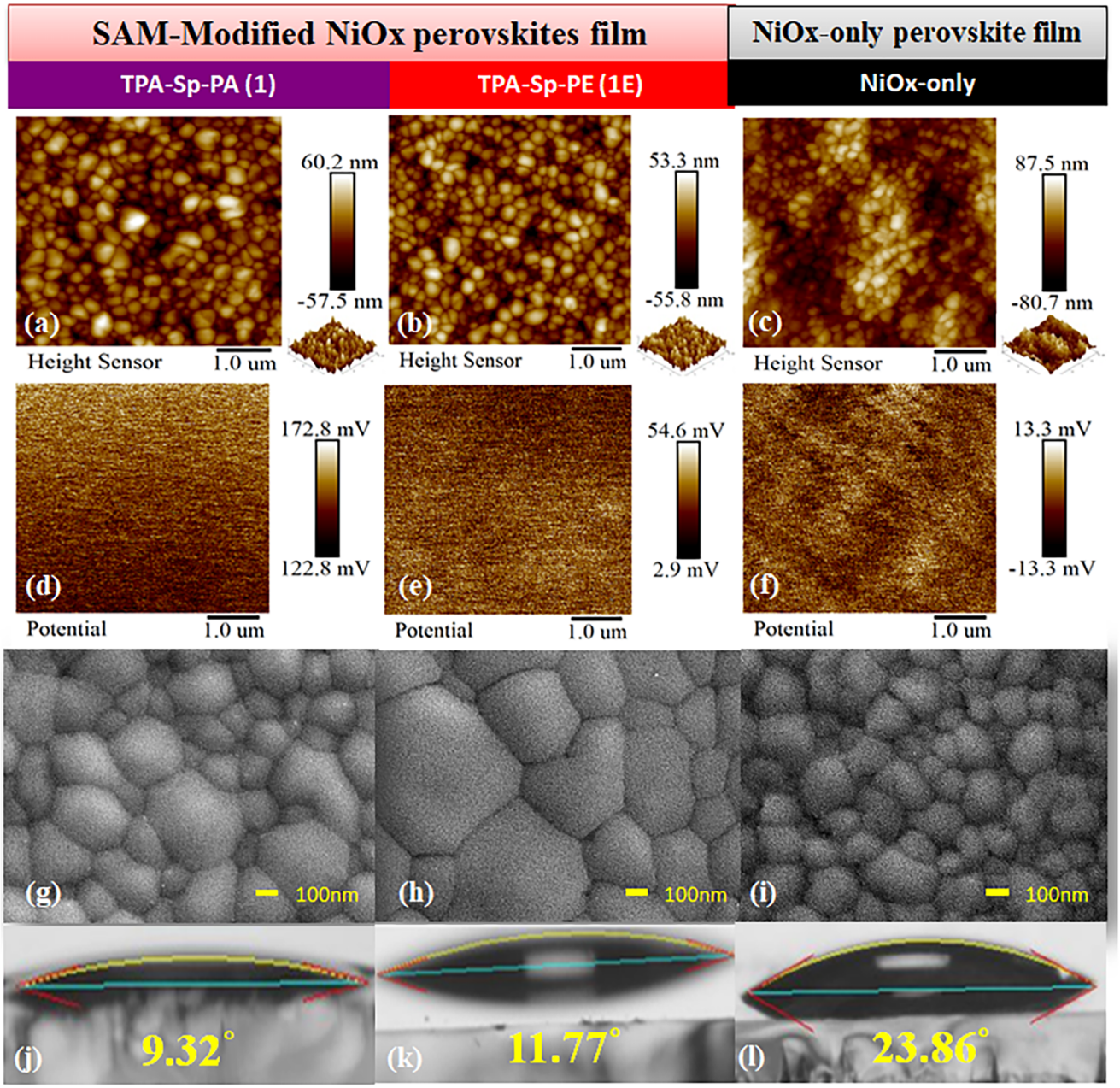

Figure 5. Thin film characterization tin perovskite made on **1**/NiOx, **1E**/NiOx, **NiOx-only** surfaces. a–c) AFM images; d–f) KPFM potential images; g–i) SEM top-view images; j–l) contact angles by using SnI_2 precursor solution.

stretching vibration when compared to pure **TPA-Sp-PE (1E)**, further supporting the specific interaction at the P═O site.[63–65]

2.6. Thin-Film Characterizations

The morphology of the tin perovskite is significantly related to the fill factor of the solar cell, and it will also determine the device's performance. We utilized atomic force microscopy (AFM) and scanning electron microscopy (SEM) to observe the morphologies of the tin perovskite films deposited on various NiOx/SAMs. **Figure** 5a–c show AFM images of the SAMs **1**/NiOx, **1E**/NiOx, and NiOx-only films, respectively, while Figure S34 (Supporting Information) shows AFM images of **2**/NiOx, **2E**/NiOx, **3**/NiOx, and **3E**/NiOx films, respectively, all deposited on the ITO substrates with the 3D images shown in the lower right corners. We can examine the roughness of the tin perovskite by the AFM analysis, for which the roughnesses of SAMs **1**, **1E**, **2**, **2E**, **3**, and **3E** on NiOx/ITO are 13.4, 12.6, 17.2, 13.5, 17.7, and 17.1 nm, respectively. The roughness of only NiOx/ITO film is 20.1 nm, demonstrating that NiOx with perovskites based on **TPA-Sp-PE (1E)** had less roughness film than the others. Figure S35

(Supporting Information) displays AFM images of the SAMs deposited on the ITO without NiOx, the roughnesses of SAMs **1**, **1E**, **2**, **2E**, **3**, and **3E** on ITO are 20.5, 19.2, 25.0, 20.6, 24.5, and 21.3 nm, respectively. The results indicate that **TPA-Sp-PE (1E)** also has less roughness than the others. It's worth mentioning that tin perovskite sensitized by SAM on ITO substrates exhibits a sheet-like structure, and after adding the NiOx, tin perovskite will display a spherical configuration. In a comparison of the two conditions aforementioned, the latter had a more specific surface area to support the forming of a homogeneous and regular interlayer between NiOx/ITO and perovskite. The KPFM results of SAMs **1**/NiOx, **1E**/NiOx, and NiOx-only films are shown in Figure 5d–f while those of **2**/NiOx, **2E**/NiOx,**3**/NiOx, and **3E**/NiOx films are shown in Figure S36 (Supporting Information), respectively; the corresponding potentials of SAMs on NiOx/ITO are 4.28, 5.63, 4.50, 5.45, 3.24, and 5.54 mV, respectively; the potential of the NiOx/ITO only film is 3.44 mV. It is apparent that the potential of **TPA-Sp-PE (1E)** is higher than those of the other SAMs, and the strong potential roughness is thought to be less favorable for electron accumulation, which makes the surface a superior location for hole accumulation to be the ideal hole transport layer. Figures S37 and S38 (Supporting Information) provide KPFM images of SAMs deposited on NiOx/ITO (Figure S37, Supporting Information) and ITO (Figure S38, Supporting Information) substrates, the nanoscale size of NiOx allows it to fill the microscopic gaps and irregularities present on the ITO surface effectively. This modification can obtain a uniform and high-quality tin perovskite layer, which is key to the optimal performance of TPSCs. Top-view SEM images of the perovskite films on various NiOx/SAMs are depicted in Figure 5g–i and Figure S39 (Supporting Information), respectively. Cross-section SEM images of the perovskite films on various NiOx/SAMs are illustrated in Figure S40 (Supporting Information). In comparison to the perovskites grown on other SAMs, it is evident that the perovskite produced by **TPA-Sp-PE(1E)** has larger and more densely packed grains with greater film thickness (360 nm). Additionally, the grain sizes match those shown in the AFM images.

The hydrophobicity of the SAM film plays a pivotal role in the fabrication of the solar cell. However, SAMs do not consistently exhibit hydrophilic properties. To tackle this challenge, our team has introduced NiOx as a modifying layer, we expect that it can promote the oxidation between the boundary of the NiOx and the perovskite layer, and generate an impediment that will obstruct the hole extraction. We employed NiOx in order to reinforce the hydrophilicity of the SAMs. The contact angles for the SAM without NiOx are illustrated in Figure S41 (Supporting Information). After the pretreatment of the NiOx deposition, the contact angles decrease for **TPA-Sp-PA** (9.32°), **TPA-Sp-PE** (11.77°), **TPA-T-PA** (11.02°), **TPA-T-PE** (12.16°), **TPA-P-PA** (10.30°), and **TPA-P-PE** (13.82°) as shown in Figure 5j,k and Figure S42 (Supporting Information); the contact angle of the NiOx-only film (23.86°) is displayed in Figure 5l. The significant decrease in contact angles proves that NiOx can improve the hydrophilicity of the SAM films. The values of the contact angle can be considered to the accessibility of the precursor solution. If it has a large value, it will be unfavorable for the deposition of perovskite because of the surface tension effect. The proper hydrophilicity of the surface can ameliorate the deposition of FAI to form $FASnI_3$ which can attain better film morphology, consequently giving better performance of the device.

2.7. Electronic and Photovoltaic Properties

It is commonly known that the perovskite active layer's structure can be utilized to control solar cell quality. We applied X-ray diffraction (XRD) patterns to ascertain the shift of the diffraction peaks and the change in intensity. The XRD patterns of tin perovskites with different SAMs deposited on NiOx are displayed in **Figure 6a**. The primary peak of the perovskites is located at 14° representing the miller index (100). **TPA-Sp-PE(1E)** has the maximum magnitude of this peak, indicating that its quality is superior to those of the other tin perovskites. In order to obtain additional validation, we conducted grazing incidence wide-angle X-ray scattering (GIWAXS) measurements. Figure 6b illustrates the organization and crystallinity of perovskites deposited on **NiOx/TPA-Sp-PE(1E)** sheet at a GIWAXS incidence angle of 0.02°; the GIWAXS results for other materials are shown in Figure S43 (Supporting Information). The predominant crystallographic orientation with regard to the substrate is indicated by diffraction intensity condensed in spots, whereas arbitrarily oriented crystals are indicated by diffraction intensity dispersed out over rings.[66] The improved crystallinity observed in the **NiOx/TPA-Sp-PE (1E)** film suggests its enhanced carrier transport and better overall device performance.

The process that turns the carrier into an electron or a hole is called charge extraction. To measure this property, tin perovskite films formed on various SAMs from the glass side with excitation at 635 nm using the time-correlated single-photon counting (TCSPC) technique; the corresponding PL decay profiles are shown in Figure 6c and the fitting parameters are displayed in Table S6 (Supporting Information). The decay profiles show that **NiOx/TPA-Sp-PE(1E)** has the greatest hole-extraction rate, demonstrating the film's excellent hole-extraction capability. Charge extraction effects, radiative recombination (bi-exponential decay), and nonradiative surface-bulk recombination (monoexponential decay) can all be used to estimate how the photoluminescence will decline. In the first period, electron transport from the bulk into the C_{60} was dominant for shorter delay durations, whereas interfacial recombination dominated the second interval.[67] Even with the quickest hole-extraction rate, hole mobility must be taken into account. Using space-charge limited current (SCLC) measurements, we calculate the hole mobility. For steady-state electron beam transfer over solar cells, the highest current density permitted is referred to as space-charge-limited electron flow.[68] Figure 6d shows that **NiOx/TPA-Sp-PE (1E)** has the best hole mobility among the other NiOx/SAM films, indicating its superior performance over the other SAMs.

We performed electrochemical impedance spectroscopy (EIS) measurements in the dark with open circuit voltage (V_{OC}) as a bias to determine the charge recombination characteristics. The barrier of charge recombination is indicated by the single semicircle of impendence, displayed in Figure 6e. It implies that the device will have better performance when the charge recombination resistance is greater, indicating the retarded charge recombination. The charge recombination resistances show the order of **NiOx/TPA-Sp-PE(1E)** > **NiOx/TPA-Sp-PA(1)**

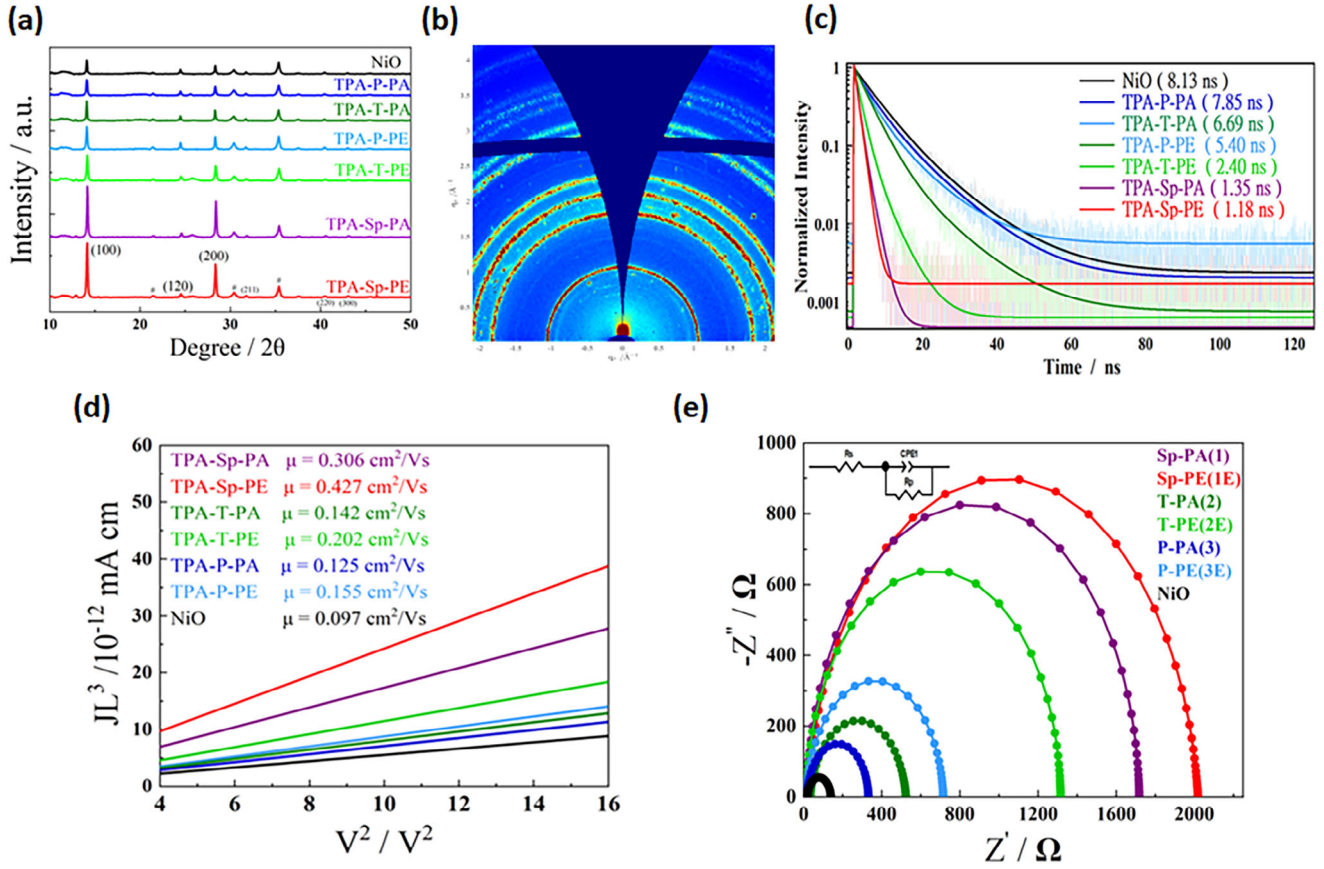

Figure 6. a) XRD patterns of tin perovskites on NiOx using various SAMs as described; b) GIWAXS figure of tin perovskite with **TPA-Sp-PE(1E)**; c) TCSPC result for PL decay; d) SCLC investigations of tin perovskites based on a variety specified SAMs over the NiOx surface; e) EIS Nyquist plots for devices made of the SAM-deposited tin perovskites on NiOx.

> **NiOx/TPA-T-PE(2E)** > **NiOx/TPA-P-PE(3E)** > **NiOx/TPA-T-PA(2)** > **NiOx/TPA-P-PA(3)** > NiOx-only as shown in Figure 6e, which is consistent with the trend of their V_{OC} values.

Matching the energy levels between perovskites and the hole transport layer is crucial for determining material suitability. We utilized ultraviolet photoelectron spectroscopy (UPS) to calculate the valence band maximum (VBM) energy levels of NiOx/SAM and only SAM as shown in **Figures** 7a and S44 (Supporting Information), respectively. The UPS raw data, with and without NiOx, are illustrated in Figures S45 and S46 (Supporting Information), respectively. The energy level of the VBM of the hole transport layer should be between the VBM of the ITO substrate and tin perovskite. Our findings indicate that the VBM of the SAMs increases after NiOx modification. Notably, the energy level of the **NiOx/TPA-Sp-PE(1E)** film perfectly matches the energy level of the tin perovskite, which accounts for its exceptional performance of the device.

The device performances made of NiOx/SAMs are shown as the *J-V* characteristic in Figure 7b and the corresponding photovoltaic parameters are displayed in Table S5 (Supporting Information). NiOx-only was selected as the reference HTM in order to compare with the other TPA-Ar-based series HTMs. The device performances follow the following order with the trend **TPA-Sp-PE** (8.73%) > **TPA-Sp-PA** (8.32%) > **TPA-T-PE** (6.59%) > **TPA-P-PE** (5.66%) > **TPA-T-PA** (5.15%) > **TPA-P-PA** (4.18%) > NiOx-only (3.05%). As shown in Figure S47 (Supporting Information), the champion device **TPA-Sp-PE (1E)** exhibits nearly no hysteresis. Figure S48 (Supporting Information) shows the incident photon-to-current conversion efficiency (IPCE) spectra and the integrated short-circuit current densities (J_{SC}) for the TPA-Ar-based devices, which provides strong support for the results obtained from the *J-V* curves (Figure 7a). The high short-circuit current density of the **NiOx/TPA-Sp-PE(1E)** device is especially noteworthy because it corresponds with its IPCE responses and represents its absorption profile, notably in the 350–700 nm spectral range (Figure S49, Supporting Information). Similarly, the morphology of the tin perovskite film allows us to determine its performance. According to the AFM figure (Figure 5a–c) and SEM image (Figure 5g–i), the devices containing selenium had less roughness and greater grain sizes, which contributed to their high performance. Moreover, we can observe by KPFM that **TPA-Sp-PE (1E)** has a higher potential to transfer holes than the others. Furthermore, **TPA-Sp-PE(1E)** reinforces hole mobility (Figure 6d) and possesses quick hole extraction (Figure 6c).

Stability is crucial for solar cell performance. In this study, we assess two types of stability to evaluate efficiency stability. Figure 7c shows the shelf-storage performance of tin perovskite solar cells with different NiOx/SAMs. Among all TPA-Ar-based

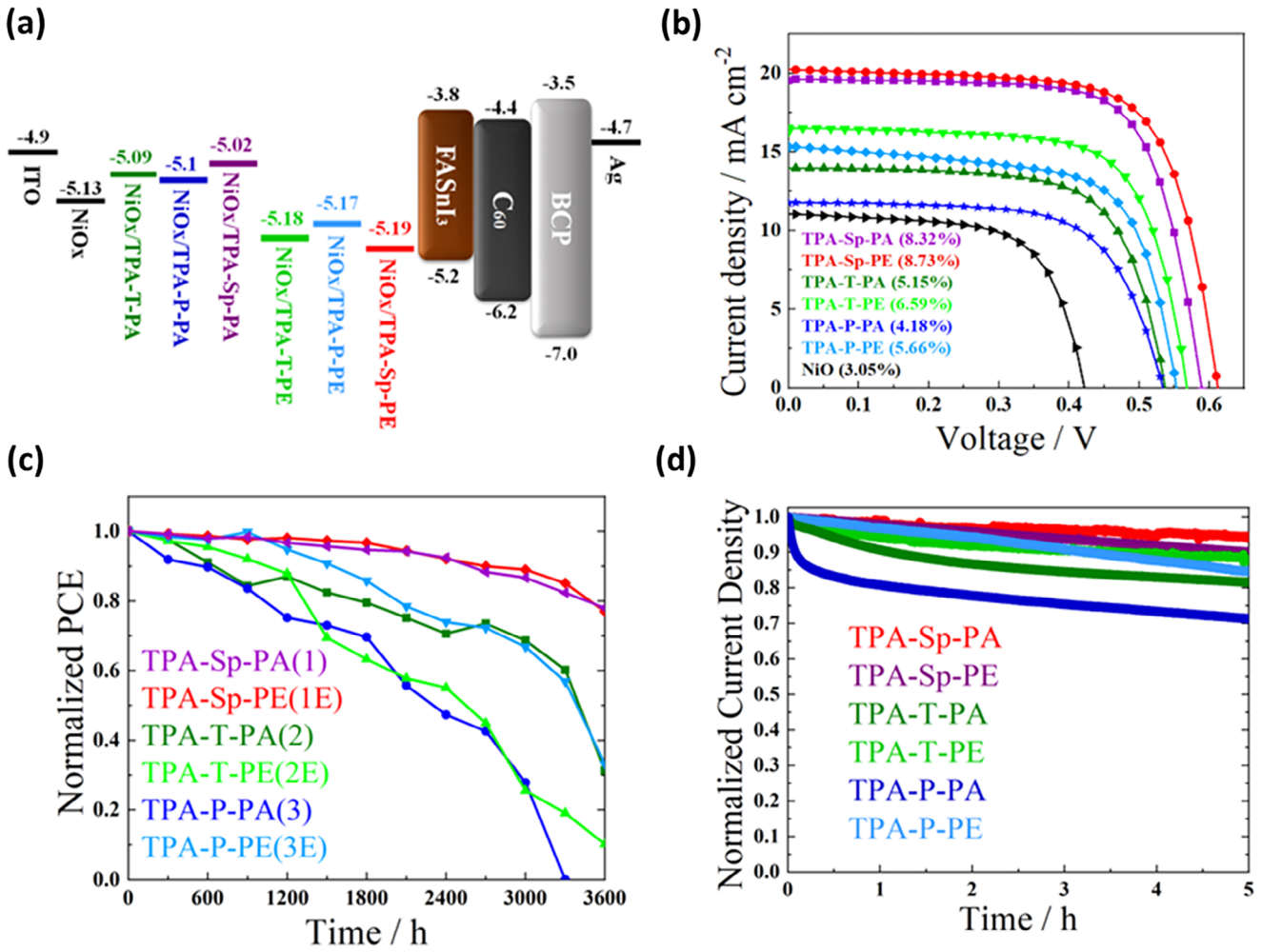

Figure 7. a) Energy-level diagram for NiOx/ SAM devices; b) IV curve of devices with various SAM on NiOx as described; c) long-term stability of the devices with various SAMs on NiOx; d) MPPT results of devices with different SAMs on NiOx.

TPSCs, the **NiOx/TPA-Sp-PE** and **NiOx/TPA-Sp-PA** devices exhibit exceptional long-term stability, retaining ≈80% of their original efficiency for over 3600 h. This stability correlates with their superior morphology, crystallinity, hole mobility, and optoelectronic properties. Another stability test was performed at the maximum power point tracking (MPPT), using a solar simulator under one sun illumination in ambient conditions. It shows that the **TPA-Sp-PE(1E)** device remains 93% of its original PCE for 5 h, as depicted in Figure 7d. Figure S50 (Supporting Information) compares the performance of SAM devices with and without a NiOx interlayer. Results reveal that NiOx-modified SAM devices outperform those without the NiOx layer. The reproducibility of these results was confirmed through performance statistics of 25 devices for each SAM, with the raw data summarized in Tables S7–S12 (Supporting Information) and boxplots shown in Figure S51 (Supporting Information).

3. Conclusion

Six novel aryl and end-group-functionalized small organic molecules—**TPA-Sp-PA** (**1**), **TPA-Sp-PE** (**1E**), **TPA-T-PA** (**2**), **TPA-T-PE** (**2E**), **TPA-P-PA** (**3**), and **TPA-P-PE** (**3E**)—were synthesized as SAMs for TPSCs. DFT computations demonstrated that the strategic placement of triphenylamine units on one side of the aryl units promoted effective charge transfer in TPSCs. Meanwhile, the PE and PA units on the other side ensured strong interactions with the NiOx/ITO surface. NiOx played a crucial role in enhancing the surface texture and hydrophilicity of the ITO substrate, supporting the formation of uniform SAMs. Single-crystal structures of **TPA-Sp-PE** (**1E**) and **TPA-T-PE** (**2E**) revealed enhanced π-conjugation, noncovalent confirmational locks, and optimal interplanar angles that promoted uniform and dense SAM layers, thereby improving charge transport. The anchoring ability of PE and PA groups across all six molecules enabled the formation of high-quality and uniform tin perovskite films with exceptional morphology and crystallinity. Devices using only NiOx as the HTM yielded a low PCE of 3.05%. However, the integration of the novel organic SAMs with NiOx significantly improved device performance, achieving remarkable PCEs of 8.32% and 8.73% for NiOx/**TPA-Sp-PA** (**1**) and NiOx/**TPA-Sp-PE** (**1E**), respectively. Notably, devices with selenophene as the core moiety outperformed those with thiophene or benzene, with PE proving

to be a superior anchoring group compared to PA. The superior performance of NiOx/**TPA-Sp-PE** (**1E**) devices was driven by optimized surface structure, efficient charge transport, enhanced charge mobility, and retarded charge recombination. A two-step approach was employed to achieve a smooth and uniform tin perovskite layer on the SAM-modified surface to overcome the challenges of the traditional one-step deposition method. This study introduces a promising strategy for leveraging innovative organic SAM molecules integrated with NiOx HTMs to attain superior TPSC performance and enhanced stability.

[CCDC 2363466 and CCDC 2363465 contain the supplementary crystallographic data for this paper. These data can be obtained free of charge from The Cambridge Crystallographic Data Centre via www.ccdc.cam.ac.uk/data_request/cif.]

Supporting Information

Supporting Information is available from the Wiley Online Library or from the author.

Acknowledgements

Y.-S.S., A.V., and C.-H.K. contributed equally to this work. The authors express our gratitude for the assistance with GIWAXS data analysis given by Drs. Y.-W. Tsai and J.-M. Lin at TPS 25A1, NSRRC. The authors are thankful for the insightful help with UPS and XPS data analysis provided by Drs. B.-H. Liu and C.-H. Wang (TLS 24A1, NSRRC). The authors are also grateful to Dr. Y.-C. Lee and Ms. P.-Y. Huang (TLS 14A1, NSRRC) for their valuable assistance with IR data analysis. The authors appreciate Pei-Lin Chen (Instrumentation Center at NTHU) for Single Crystal X-ray Diffractometer analysis. The authors gratefully acknowledge the support by the National Science and Technology Council (NSTC), Taiwan (grant No. NSTC 111-2622-8-008-006, NSTC 112-2639-M-A49-001-ASP and NSTC 113-2639-M-A49-001-ASP), and the Center for Emergent Functional Matter Science of National Yang-Ming Chiao-Tung University (NYCU) from the Featured Areas Research Center Program within the framework of the Higher Education Sprout Project by the Ministry of Education (MOE) in Taiwan. M.-C. Chen also gratefully acknowledges the funding provided by the NCU-Covestro Research Center.

Conflict of Interest

The authors declare no conflict of interest.

Data Availability Statement

The data that support the findings of this study are available from the corresponding author upon reasonable request.

Keywords

heteroatom, selenophene, self-assembled monolayer, tin perovskite solar cells, two-step fabrication

Received: January 16, 2025
Revised: February 13, 2025
Published online:

[1] Y. Bai, Z. Zhou, Q. Xue, C. Liu, N. Li, H. Tang, J. Zhang, X. Xia, J. Zhang, X. Lu, C. J. Brabec, F. Huang, *Adv. Mater.* **2022**, *34*, 2110587.
[2] G. Szabó, N.-G. Park, F. De Angelis, P. V. Kamat, *ACS Energy Lett.* **2023**, *8*, 3829.
[3] S. Liu, J. Li, W. Xiao, R. Chen, Z. Sun, Y. Zhang, X. Lei, S. Hu, M. Kober-Czerny, J. Wang, F. Ren, Q. Zhou, H. Raza, Y. Gao, Y. Ji, S. Li, H. Li, L. Qiu, W. Huang, Y. Zhao, B. Xu, Z. Liu, H. J. Snaith, N.-G. Park, W. Chen, *Nature* **2024**, *632*, 536.
[4] A. Velusamy, S. Yau, C.-L. Liu, Y. Ezhumalai, P. Kumaresan, M.-C. Chen, *J. Chin. Chem. Soc.* **2023**, *70*, 2046.
[5] N. Tiwari, H. Arianita Dewi, E. Erdenebileg, R. Narayan Chauhan, N. Mathews, S. Mhaisalkar, A. Bruno, *Sol. RRL* **2022**, *6*, 2100700.
[6] X. Yin, Y. Guo, H. Xie, W. Que, L. B. Kong, *Sol. RRL* **2019**, *3*, 1900001.
[7] A. Velusamy, S. N. Afraj, Y.-S. Guo, J.-S. Ni, H.-L. Huang, T.-Y. Su, Y. Ezhumalai, C.-L. Liu, C.-H. Chiang, M.-C. Chen, C.-G. Wu, *ACS Appl. Mater. Interfaces* **2024**, *16*, 6162.
[8] W. Chen, F.-Z. Liu, X.-Y. Feng, A. B. Djurišić, W. K. Chan, Z.-B. He, *Adv. Energy Mater.* **2017**, *7*, 1700722.
[9] W. Chen, G. Pang, Y. Zhou, Y. Sun, F.-Z. Liu, R. Chen, S. Chen, A. B. Djurišić, Z. He, *J. Mater. Chem. A* **2020**, *8*, 1865.
[10] Y. Kim, E. H. Jung, G. Kim, D. Kim, B. J. Kim, J. Seo, *Adv. Energy Mater.* **2018**, *8*, 1801668.
[11] M. Wang, H. Wang, W. Li, X. Hu, K. Sun, Z. Zang, *J. Mater. Chem. A* **2019**, *7*, 26421.
[12] W. Han, G. Ren, J. Liu, Z. Li, H. Bao, C. Liu, W. Guo, *ACS Appl. Mater. Interfaces* **2020**, *12*, 49297.
[13] J.-Y. Jeng, K.-C. Chen, T.-Y. Chiang, P.-Y. Lin, T.-D. Tsai, Y.-C. Chang, T.-F. Guo, P. Chen, T.-C. Wen, Y.-J. Hsu, *Adv. Mater.* **2014**, *26*, 4107.
[14] J. Seo, S. Park, Y. C Kim, N. J. Jeon, J. H. Noh, S. C. Yoon, S. I. Seok, *Energy Environ. Sci.* **2014**, *7*, 2642.
[15] S. Wang, H. Guo, Y. Wu, *Mater. Futures* **2023**, *2*, 012105.
[16] X. Jiang, Z. Yu, Y. Zhang, J. Lai, J. Li, G. G. Gurzadyan, X. Yang, L. Sun, *Sci. Rep.* **2017**, *7*, 42564.
[17] F. Zhang, Z. Yao, Y. Guo, Y. Li, J. Bergstrand, C. J. Brett, B. Cai, A. Hajian, Y. Guo, X. Yang, J. M. Gardner, J. Widengren, S. V. Roth, L. Kloo, L. Sun, *J. Am. Chem. Soc.* **2019**, *141*, 19700.
[18] A. Batdelger, S.-G. Lee, S.-G. Park, *ChemElectroChem* **2023**, *10*, 202300040.
[19] K. Almasabi, X. Zheng, B. Turedi, A. Y. Alsalloum, M. N. Lintangpradipto, J. Yin, L. Gutiérrez-Arzaluz, K. Kotsovos, A. Jamal, I. Gereige, O. F. Mohammed, O. M. Bakr, *ACS Energy Lett.* **2023**, *8*, 950.
[20] Z. Wang, H. Lin, X. Zhang, J. Li, X. Chen, S. Wang, W. Gong, H. Yan, Q. Zhao, W. Lv, X. Gong, Q. Xiao, F. Li, D. Ji, X. Zhang, H. Dong, L. Li, W. Hu, *Sci. Adv.* **2021**, *7*, eabf8555.
[21] R. Azmi, W. T. Hadmojo, S. Sinaga, C.-L. Lee, S. C. Yoon, I. H. Jung, S.-Y. Jang, *Adv. Energy Mater.* **2018**, *8*, 1701683.
[22] S. Y. Kim, S. J. Cho, S. E. Byeon, X. He, H. J. Yoon, *Adv. Energy Mater.* **2020**, *10*, 2002606.
[23] F. Ali, C. Roldán-Carmona, M. Sohail, M. K. Nazeeruddin, *Adv. Energy Mater.* **2020**, *10*, 2002989.
[24] Y. Yao, C. Cheng, C. Zhang, H. Hu, K. Wang, S. De Wolf, *Adv. Mater.* **2022**, *34*, 2203794.
[25] G.-H. Kim, F. P. García de Arquer, Y. J. Yoon, X. Lan, M. Liu, O. Voznyy, Z. Yang, F. Fan, A. H. Ip, P. Kanjanaboos, S. Hoogland, J. Y. Kim, E. H. Sargent, *Nano Lett.* **2015**, *15*, 7691.
[26] A. Asyuda, M. Gärtner, X. Wan, I. Burkhart, T. Saßmannshausen, A. Terfort, M. Zharnikov, *J. Phys. Chem. C* **2020**, *124*, 8775.
[27] D. Yeo, J. Shin, D. Kim, J. Y. Jaung, I. H. Jung, *Nanomaterials* **2024**, *14*, 175.
[28] F. Ambrosio, N. Martsinovich, A. Troisi, *J. Phys. Chem. Lett.* **2012**, *3*, 1531.
[29] A. Magomedov, A. Al-Ashouri, E. Kasparavičius, S. Strazdaite, G. Niaura, M. Jošt, T. Malinauskas, S. Albrecht, V. Getautis, *Adv. Energy Mater.* **2018**, *8*, 1801892.

[30] A. Al-Ashouri, A. Magomedov, M. Roß, M. Jošt, M. Talaikis, G. Chistiakova, T. Bertram, J. A. Márquez, E. Köhnen, E. Kasparavičius, S. Levcenco, L. Gil-Escrig, C. J. Hages, R. Schlatmann, B. Rech, T. Malinauskas, T. Unold, C. A. Kaufmann, L. Korte, G. Niaura, V. Getautis, S. Albrecht, *Energy Environ. Sci.* **2019**, *12*, 3356.
[31] E. Li, C. Liu, H. Lin, X. Xu, S. Liu, S. Zhang, M. Yu, X.-M. Cao, Y. Wu, W.-H. Zhu, *Adv. Funct. Mater.* **2021**, *31*, 2103847.
[32] A. Ullah, K. H. Park, H. D. Nguyen, Y. Siddique, S. F. A. Shah, H. Tran, S. Park, S. I. Lee, K.-K. Lee, C.-H. Han, K. Kim, S. Ahn, I. Jeong, Y. S. Park, S. Hong, *Adv. Energy Mater.* **2022**, *12*, 2103175.
[33] W. Jiang, F. Li, M. Li, F. Qi, F. R. Lin, A. K.-Y. Jen, *Angew. Chem., Int. Ed.* **2022**, *61*, 202213560.
[34] J. Wu, P. Yan, D. Yang, H. Guan, S. Yang, X. Cao, X. Liao, P. Ding, H. Sun, Z. Ge, *Adv. Mater.* **2024**, *36*, 2401537.
[35] S. Zhang, F. Ye, X. Wang, R. Chen, H. Zhang, L. Zhan, X. Jiang, Y. Li, X. Ji, S. Liu, M. Yu, F. Yu, Y. Zhang, R. Wu, Z. Liu, Z. Ning, D. Neher, L. Han, Y. Lin, H. Tian, W. Chen, M. Stolterfoht, L. Zhang, W.-H. Zhu, Y. Wu, *Science* **2023**, *380*, 404.
[36] Y. Shi, Z. Zhu, D. Miao, Y. Ding, Q. Mi, *ACS Energy Lett.* **2024**, *9*, 1895.
[37] J. Chen, J. Luo, E. Hou, P. Song, Y. Li, C. Sun, W. Feng, S. Cheng, H. Zhang, L. Xie, C. Tian, Z. Wei, *Nat. Photonics* **2024**, *18*, 464.
[38] N. Sun, W. Gao, H. Dong, Y. Liu, X. Liu, Z. Wu, L. Song, C. Ran, Y. Chen, *ACS Energy Lett.* **2021**, *6*, 2863.
[39] E. Jokar, H.-S. Chuang, C.-H. Kuan, H.-P. Wu, C.-H. Hou, J.-J. Shyue, E. Wei-Guang Diau, *J. Phys. Chem. Lett.* **2021**, *12*, 10106.
[40] X. Jiang, F. Wang, Q. Wei, H. Li, Y. Shang, W. Zhou, C. Wang, P. Cheng, Q. Chen, L. Chen, Z. Ning, *Nat. Commun.* **2020**, *11*, 1245.
[41] X. Jiang, Z. Zang, Y. Zhou, H. Li, Q. Wei, Z. Ning, *Acc. Mater. Res.* **2021**, *2*, 210.
[42] E. Jokar, P.-Y. Cheng, C.-Y. Lin, S. Narra, S. Shahbazi, E. Wei-Guang Diau, *ACS Energy Lett.* **2021**, *6*, 485.
[43] E. Jokar, P.-H. Hou, S. S. Bhosale, H.-S. Chuang, S. Narra, E. Wei-Guang Diau, *ChemSusChem* **2021**, *14*, 4415.
[44] E. Jokar, Z. Y. Huang, S. Narra, C.-Y. Wang, V. Kattoor, C.-C. Chung, E. W.-G. Diau, *Adv. Energy Mater.* **2018**, *8*, 1701640.
[45] C.-M. Tsai, Y.-P. Lin, M. K. Pola, S. Narra, E. Jokar, Y.-W. Yang, E. W.-G. Diau, *ACS Energy Lett.* **2018**, *3*, 2077.
[46] S. Narra, C.-Y. Lin, A. Seetharaman, E. Jokar, E. W.-G. Diau, *J. Phys. Chem. Lett.* **2021**, *12*, 12292.
[47] R. Balasaravanan, C.-H. Kuan, S.-M. Hsu, E.-C. Chang, Y.-C. Chen, Y.-T. Tsai, M.-L. Jhou, S.-L. Yau, C.-L. Liu, M.-C. Chen, E. W.-G. Diau, *Adv. Energy Mater.* **2023**, *13*, 2302047.
[48] C.-H. Kuan, R. Balasaravanan, S.-M. Hsu, J.-S. Ni, Y.-T. Tsai, Z.-X. Zhang, M.-C. Chen, E. W.-G. Diau, *Adv. Mater.* **2023**, *35*, 2300681.
[49] D. Song, S. Narra, M.-Y. Li, J.-S. Lin, E. W.-G. Diau, *ACS Energy Lett.* **2021**, *6*, 4179.
[50] C.-H. Kuan, S. N. Afraj, Y.-L. Huang, A. Velusamy, C.-L. Liu, T.-Y. Su, X. Jiang, J.-M. Lin, M.-C. Chen, E. W.-G. Diau, *Angew. Chem., Int. Ed.* **2024**, *136*, 202407228.
[51] S. N. Afraj, C.-H. Kuan, J.-S. Lin, J.-S. Ni, A. Velusamy, M.-C. Chen, E. W.-G. Diau, *Adv. Funct. Mater.* **2023**, *33*, 2213939.
[52] S. N. Afraj, C.-H. Kuan, H.-L. Cheng, Y.-X. Wang, C.-L. Liu, Y.-S. Shih, J.-M. Lin, Y.-W. Tsai, M.-C. Chen, E. W.-G. Diau, *Small* **2024**, 2408638.
[53] Z. Yi, X. Li, Y. Xiong, G. Shen, W. Zhang, Y. Huang, Q. Jiang, X. R. Ng, Y. Luo, J. Zheng, W. L. Leong, F. Fu, T. Bu, J. Yang, *Interdiscip. Mater.* **2024**, *3*, 203.
[54] Y. Diao, L. Shaw, Z. Bao, S. C. B. Mannsfeld, *Energy Environ. Sci.* **2014**, *7*, 2145.
[55] A. Velusamy, Y.-Y. Chen, M.-H. Lin, S. N. Afraj, J.-H. Liu, M.-C. Chen, C.-L. Liu, *Adv. Sci.* **2024**, *11*, 2305361.
[56] S. N. Afraj, A. Velusamy, M.-C. Chen, M. Abd-Ella, A. L. Abdelhady, *Coord. Chem. Rev.* **2025**, *532*, 216500.
[57] S. Shahbazi, M.-Y. Li, A. Fathi, E. W.-G. Diau, *ACS Energy Lett.* **2020**, *5*, 2508.
[58] A. Velusamy, C.-H. Yu, S. N. Afraj, C.-C. Lin, W.-Y. Lo, C.-J. Yeh, Y.-W. Wu, H.-C. Hsieh, J. Chen, G.-H. Lee, S.-H. Tung, C.-L. Liu, M.-C. Chen, A. Facchetti, *Adv. Sci.* **2021**, *8*, 2002930.
[59] M. Du, S. Zhao, L. Duan, Y. Cao, H. Wang, Y. Sun, L. Wang, X. Zhu, J. Feng, L. Liu, X. Jiang, Q. Dong, Y. Shi, K. Wang, S. Liu, *Joule* **2022**, *6*, 1931.
[60] S. Yu, Z. Xiong, H. Zhou, Q. Zhang, Z. Wang, F. Ma, Z. Qu, Y. Zhao, X. Chu, X. Zhang, J. You, *Science* **2023**, *382*, 1399.
[61] X. Cui, J. Jin, J. Zou, Q. Tang, Y. Ai, X. Zhang, Z. Wang, Y. Zhou, Z. Zhu, G. Tang, Q. Cao, S. Liu, X. Liu, Q. Tai, *Adv. Funct. Mater.* **2022**, *32*, 2203049.
[62] C. Gao, H. Zhang, F. Qiao, H. Huang, D. Zhang, D. Ding, D. Du, J. Liang, J. Bao, H. Liu, W. Shen, *Nano Energy* **2023**, *116*, 108765.
[63] Q. Cao, T. Wang, X. Pu, X. He, M. Xiao, H. Chen, L. Zhuang, Q. Wei, H.-L. Loi, P. Guo, B. Kang, G. Feng, J. Zhuang, G. Feng, X. Li, F. Yan, *Adv. Mater.* **2024**, *36*, 2311970.
[64] H. Chen, W. Zhang, M. Li, G. He, X. Guo, *Chem. Rev.* **2020**, *120*, 2879.
[65] C. Quefféléc, M. Petit, P. Janvier, D. A. Knight, B. Bujoli, *Chem. Rev.* **2012**, *112*, 3777.
[66] A. Z. Chen, M. Shiu, J. H. Ma, M. R. Alpert, D. Zhang, B. J. Foley, D.-M. Smilgies, S.-H. Lee, J. J. Choi, *Nat. Commun.* **2018**, *9*, 1336.
[67] H. Chen, C. Liu, J. Xu, A. Maxwell, W. Zhou, Y. Yang, Q. Zhou, A. S. R. Bati, H. Wan, Z. Wang, L. Zeng, J. Wang, P. Serles, Y. Liu, S. Teale, Y. Liu, M. I. Saidaminov, M. Li, N. Rolston, S. Hoogland, T. Filleter, M. G. Kanatzidis, B. Chen, Z. Ning, E. H. Sargent, *Science* **2024**, *384*, 189.
[68] Y. Zhu, in *Modeling of space charge limited current*, Nanyang Technological University, Singapore **2014**.